*Networks and Heterogeneous Media*

*Research article*

# Dynamic strain gradient brittle fracture propagation: comparison with experimental evidence

**Valerii Maksimov[1], Luca Placidi[1,*], Francisco James León Trujillo[2], Chiara De Santis[3], Anil Misra[4], Dmitry Timofeev[2], Francesco Fabbrocino[5] and Emilio Barchiesi[2,3]**

[1] Faculty of Engineering, International Telematic University Uninettuno, Rome, Italy

[2] International Research Center on Mathematics and Mechanics of Complex Systems (M&MoCS), Università degli Studi dell'Aquila, L'Aquila, Italy

[3] Department of architecture, design and urbanism, Università degli Studi di Sassari, Alghero, Italy

[4] Department of Civil and Environmental Engineering, Florida International University, Miami, FL, USA

[5] Faculty of Engineering, Telematic University Pegaso, Naples, Italy

* **Correspondence:** Email: luca.placidi@uninettunouniversity.net.

**Abstract:** This paper presented a physico-mathematical model for dynamic fracture propagation in brittle materials with a purely continuum mechanics hemi-variational-based strain gradient theory. As for the quasi-static case, the simulation results, obtained by means of finite elements, revealed that strain gradient effects significantly affected the fracture propagation, leading to finite fracture thickness that was independent of the mesh size. It was also observed that nonsymmetric loading rate lead to a deviation from standard mode-I crack propagation that cannot be revealed in the quasi-static case. The model results were compared against experimental data from fracture tests on notched specimens taken from the literature. The comparison showed good agreement between the model predictions and the experimental measurements. The presented model and simulation results can be useful in the design and optimization of structural components subjected to dynamic loading conditions.

**Keywords:** strain gradient; 2D continua; damage mechanics; variational procedure; kinetic energy; Karush-Kuhn-Tucker conditions

## 1. Introduction

Fracture mechanics is a fundamental field of study in mechanical sciences. Over the years, extensive research has focused on studying fracture processes under static loading conditions, providing valuable

insights into crack initiation, propagation, and structural failure. However, in many real-world scenarios, materials are subjected to dynamic loading conditions, where cracks can propagate at high speeds and exhibit unique fracture behaviors [7, 39, 43, 45, 64, 73, 77, 80]. Understanding the mechanics of dynamic fracture is hence crucial for enhancing the safety and reliability of structural components and advancing the design of resilient materials. The mechanics underlying dynamic fractures presents many more intricacies than underlying quasi-static fracture [58–61]. Experimental studies, however, show its practical relevance [6, 17, 20, 23, 25, 68, 79, 81] and also elucidate its loading rate-dependent behavior [18, 24, 26, 27, 30, 40, 44, 70, 72, 78]. More specifically, the study of dynamic fracture finds application in engineering [8, 18, 54], automotive safety [33], medicine [69], material science [28], and biology [74]. Examples of dynamic fracture events include rapid crack propagation in structural components under time-dependent loading due to, e.g., impacts, explosions, or earthquakes [24], fragmentation of brittle materials under high-velocity impacts, and crack propagation in geological formations due to seismic activity. The study of dynamic fracture mechanics aims to unravel the underlying mechanisms governing the initiation, propagation, and arrest of cracks under these extreme loading conditions.

This paper presents a physico-mathematical model that addresses dynamic fracture propagation in brittle materials by applying a purely hemi-variational continuum mechanics-based strain gradient theory. This paper is based on experimental analyses conducted in [41], which delved into the dependence of the fracture path on the loading rate. In a theoretical paper aimed at predicting mathematically the fracture path and the related branching phenomena, the same authors utilized a microplane model [42] in a 3D numerical simulation. In works [5, 22, 55, 71], in order to describe the experimental results on dynamic fracture propagation reported in [41], different approaches were used like peridynamic, microplane, and phase-field damage modeling. The recent work of Nguyen et al. [38] gives a reformulation, in terms of sprain and spress, of a subset of micromorphic theories discussed more than half a century ago by Germain [21], Mindlin [34], and Eringen [16], whose micromechanical foundations for granular systems have been elaborated in a variational approach for finite deformation [36], geometrically nonlinear strain gradient models [4], and n-th order micromorphic materials [37]. Following this granular micromechanical approach and utilizing hemivariational methods, a group of researchers in a series of papers [10, 35, 47, 49, 50, 52, 67] have clearly established the physical meaning of boundary conditions associated with strain gradient theories [2, 3, 11–15, 62, 63, 66, 76]. Moreover, they have shown that for heterogeneous systems, strain gradient theories with appropriate elastic and dissipative energies can predict a multitude of phenomena, such as evolution of chirality and size of localization/fracture zone, that are oftentimes ignored or overlooked in classical approaches [9, 19, 29, 31]. The strain gradient with the inertia gradient effects approach was used in [46, 65], the treatment being purely analytical, without application of numerical methods such as the finite element method (FEM). In the papers of Rao et al. [56, 57], strain gradient effects in the modeling of fracture mechanics have been considered with a two-scale asymptotic analysis. In this study, we employ an isotropic model to investigate the behavior of experiments presented in [41]. Our objective is to tune the evolution of damage based on discerning the local strain/stress state, namely, tension/compression. Specifically, we aim at mitigating, avoiding actually, its occurrence in compression. The utilization of an isotropic model accounts for uniformity of the microstructure with respect to directions.

The paper is organized as follows. In Section 2, we introduce the strain-gradient continuum model–elastic and damage components-employed to investigate numerically the propagation of dynamic

fracture. In Section 3, we apply the presented model to an experimental case study that is then used for comparison with experimental data and other theoretical approaches available in the literature by solving through the weak form package of the software COMSOL Multiphysics and the weak form of its governing equations. Finally, conclusions are drawn in Section 4.

## 2. Formulation of the problem

### 2.1. Preliminary definitions

Let us consider a 2D continuum body $\mathfrak{B} \subset E^2$, where the domain $E^2$ is the Euclidean two-dimensional space. The position of every point in the body is established through the utilization of $X$ coordinates in a frame of reference. The set of kinematic descriptors for such a model contains both the displacement field $u = u(X, t)$ and the damage field $\omega = \omega(X, t)$. The damage state of a material point $X$ is therefore characterized, at time $t$, by a scalar internal variable $\omega$, which is assumed to take values within the range [0, 1]. The case $\omega = 0$ corresponds to the undamaged state, while $\omega = 1$ corresponds to complete failure. We assume the material to be not self-healing and, hence, $\omega$ is assumed to be a nondecreasing function of time. If we consider the material as a microstructured one, it becomes significant to allow the deformation energy density to vary based on the second gradient of the displacement. Thus, because of objectivity, the potential energy $U$ is assumed to be a function of the strain tensor $G$, of its gradient $\nabla G$, and of the damage $\omega$, i.e., $U = U(G, \nabla G, \omega)$. Here, $G = \frac{1}{2} \left( F^T F - I \right)$, where $F = \nabla \chi$ is the deformation gradient tensor, $\chi = X + u$ is the placement function, and $F^T$ is the transpose of $F$. For the small displacement approximation that is dealt with in this work, the strain tensor $G$ is assumed to be equal to $E = Sym(\nabla u)$, the symmetric part of the displacement gradient.

### 2.2. The Energy functional

The energy functional $\mathcal{E}(u, \omega)$ depends on the displacement $u$ and the damage $\omega$ and is given as follows [53]:

$$
\begin{aligned}
\mathcal{E}(u, \omega) = &\int_{\mathfrak{B}} \left[ U_e(G, \nabla G, \omega) + U_d(\omega) - b^{ext} \cdot u - m^{ext} : \nabla u \right] dA \\
&- \int_{\partial \mathfrak{B}} [t^{ext} \cdot u + \tau^{ext} \cdot [(\nabla u)n]] ds - \int_{[\partial \partial \mathfrak{B}]} f^{ext} \cdot u
\end{aligned}
\tag{2.1}
$$

where $\partial \mathfrak{B}$ are the regular parts of the boundary of $\mathfrak{B}$, the symbol $[\partial \partial \mathfrak{B}]$ denotes the regular parts of the boundary of $\partial \mathfrak{B}$, i.e., its wedges, and $n$ is the unit external normal. The symbols $(\cdot)$ and $(:)$ indicate the scalar product between vectors or tensors, respectively. The quantities $b^{ext}$ and $m^{ext}$ are, respectively, the external body force and double force (per unit area), while the quantities $t^{ext}$ and $\tau^{ext}$ are, respectively, the external force and double force (per unit length). Finally, the quantity $f^{ext}$ is the external concentrated force which is applied on the vertices $[\partial \partial \mathfrak{B}]$.

### 2.3. Variational principle

In order to get governing equations for this model, we resort to the variational principle thoroughly presented in [32, 48, 49, 51, 53, 75], where the case of one-dimensional bodies was considered. We assume that the descriptors $u(X, t)$ and $\omega(X, t)$ verify the condition

$$\delta\mathcal{E}(u, \omega, \dot{u}, \dot{\omega}) \leq \delta\mathcal{E}(u, \omega, v, \beta), \qquad \forall v, \ \forall \beta \geq 0, \tag{2.2}$$

where $v$ and $\beta$ are compatible virtual velocities and dots represent derivation with respect to time.

### 2.4. Reduction from the 3D Mindlin elastic strain gradient energy to the 2D explicit form

A general form of the deformation energy density of an elastic 3D isotropic strain gradient elastic material is provided in [34]. In our case, we have

$$U_e(G, \nabla G, \omega) = \mathbb{H}(-TrG + \gamma)(U_e^I + U_e^{II}) + \mathbb{H}(TrG - \gamma)\left[(1 - r\omega)U_e^I + (1 - m\omega)U_e^{II}\right] \tag{2.3}$$

where $\mathbb{H}$ is the Heaviside function, $TrG$ is the trace of $G$, $r$ affects on the 1st gradient residual inside the fracture, and $m$ affects on microstructure due to damage. Parameters $r$ and $m$ should be as close as possible to the value 1. $\gamma$ is a constitutive parameter representing the threshold of the trace of $G$ controlling the bi-modular behavior of damage, which stipulates that damage evolution occurs only when the trace of the strain tensor $G$ is positive and exceeds a predefined threshold. By implementing this condition, we ensure that damage progression is assessed solely in regions experiencing tensile stresses. The first gradient part $U_e^I$ of the deformation energy density above reads as

$$U_e^I(G, \nabla G) = \frac{\lambda}{2}G_{ii}G_{jj} + \mu G_{ij}G_{ij} \tag{2.4}$$

and the strain gradient part $U_e^{II}$ reads as

$$U_e^{II}(G, \nabla G, \omega) = 2c_3 G_{ii,j}G_{jh,h} + \frac{c_4}{2}G_{ii,k}G_{ll,k} + 2c_5 G_{ij,i}G_{jm,m} + c_6 G_{ij,k}G_{ij,k} + 2c_7 G_{ij,k}G_{ki,j} \tag{2.5}$$

where $\lambda, \mu, c_3, c_4, c_5, c_6, c_7 \in \mathbb{R}$ are independent parameters. Our model accounts for an isotropic material, because the key focus is on the examination of damage evolution exclusively under tension while avoiding its manifestation in compression, aimed at capturing the behavior of cementitious materials. The quantities $\lambda$ and $\mu$ in Eq (2.4) are referred to as Lamé parameters and it is a classical result in mechanics that they can be easily related to the Young modulus $Y$ and to the Poisson's ratio $v$. For the 2D case, we have

$$\lambda = \frac{Yv}{(1 + v)(1 - 2v)}, \qquad \mu = \frac{Y}{2(1 + v)}. \tag{2.6}$$

The coefficients $c_3$–$c_7$ can instead be identified in terms of Young modulus and Lamé parameters, and an internal characteristic length–also referred to as the intergranular distance–within the granular micro-mechanics-based framework presented in [4] is as follows:

$$\begin{cases} c_3 = YL^2 \frac{v}{112(1+v)(1-2v)} = \frac{L^2}{112}\lambda, \\ c_4 = YL^2 \frac{v}{112(1+v)(1-2v)} = \frac{L^2}{112}\lambda, \\ c_5 = YL^2 \frac{7-8v}{2240(1+v)(1-2v)} = \frac{L^2}{1120}(7\mu + 3\lambda), \\ c_6 = YL^2 \frac{7-18v}{1120(1+v)(1-2v)} = \frac{L^2}{1120}(7\mu - 4\lambda), \\ c_7 = YL^2 \frac{7-8v}{2240(1+v)(1-2v)} = \frac{L^2}{1120}(7\mu + 3\lambda). \end{cases} \tag{2.7}$$

We now introduce the dissipated energy $U_d$ as

$$U_d(\omega) = \frac{1}{2}k_\omega \omega^2 \tag{2.8}$$

where $k_\omega$ represents the resistance to damage. The kinetic energy $U_k$ is instead assumed to having the following expression:

$$U_k = \frac{1}{2}\rho \left\| \frac{\partial u}{\partial t} \right\|^2 = \frac{1}{2}\rho \left( \frac{\partial^2 u_1}{\partial t^2} + \frac{\partial^2 u_2}{\partial t^2} \right). \tag{2.9}$$

where $\rho$ is material density per unit area and $u_1$ and $u_2$ are the displacement components in the horizontal and vertical directions, respectively. It is easy to prove [1] that having a nonzero kinetic energy in the form above is equivalent to have $b^{ext} = -\rho \ddot{u}$.

## 3. Numerical results

The weak form package of the commercial software COMSOL Multiphysics has been employed to perform the numerical simulation presented in this section, based on the modeling presented so far.

### 3.1. Description of the numerical experiments

In the current section, we present numerical simulations to show the capabilities of the presented model to describe initiation and growth of damage localization zones. Following [41], we consider a 2D square specimen with a notch (pre-crack). The followig type of numerical experiment is considered: the left edge of the notch (the blue line) is fixed, i.e., cannot move, along the direction $\hat{e}_x$, while the right edge of the notch (the red line) is subjected to an applied velocity in the $\hat{e}_x$ direction (from left to right). Such an applied velocity will be also referred to as *crack-opening velocity*.
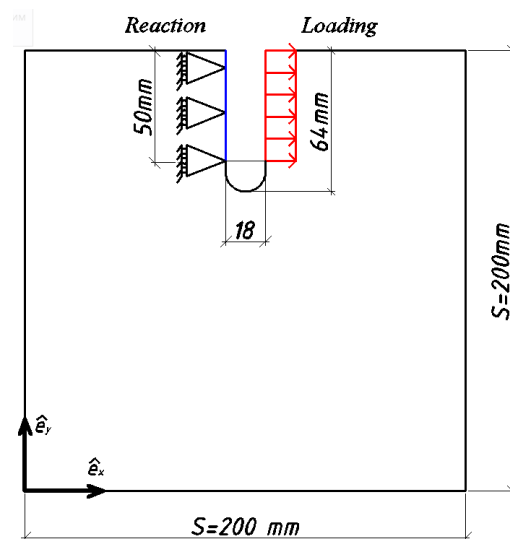


**Figure 1.** Schematics of analyzed domains and considered boundary conditions.

Figure 1 illustrates this loading condition. In the original paper [41], there are twelve cases of different applied velocities, the loading-rates being in the range from 0.045 m/s to 4.298 m/s. In this section, only

four cases of tested velocities are considered for the study, which are Case 1: 0.491 m/s; Case 2: 1.375 m/s; Case 3: 3.268 m/s, and Case 4: 4.298 m/s. In the current study, the applied velocity is assumed to depend upon time–the data of the actual loading history used in the experiments was not reported in the original paper, as follows:

$$v = \begin{cases} \frac{t}{t_0} v_0 & t \leq t_0 \\ v_0 & t > t_0 \end{cases} \tag{3.1}$$

with $t_0 = 100 \, \mu s$ and $t = 500 \, \mu s$. The prescribed displacement velocity as a function of time for $v_0 = 3.268$ m/s is reported in Figure 2.
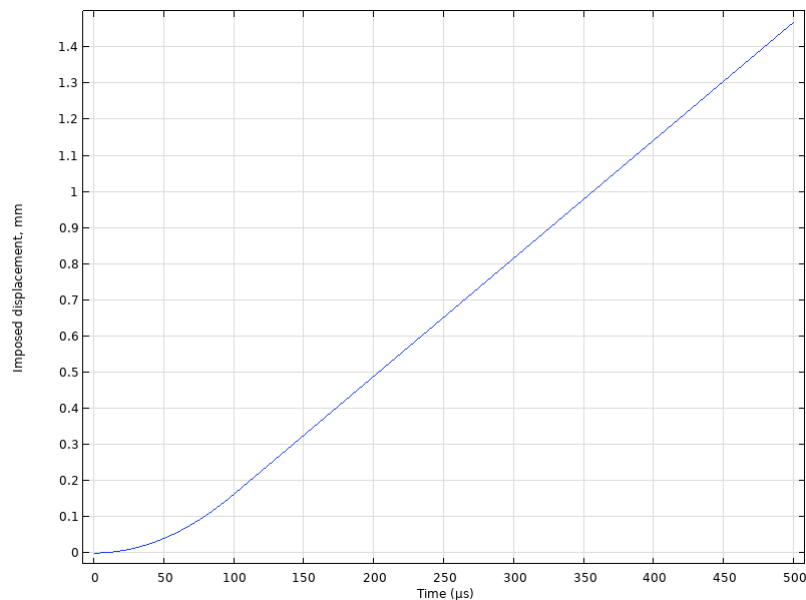


**Figure 2.** Representation of the prescribed displacement velocity versus time for $v_0 = 3.268$ m/s.

The constitutive parameters used in the numerical simulations are reported in Table 1, where $t_f$ is the time horizon of the simulations and $\triangle t$ the time step. It should be noted that since simulations were performed for the 2D case, to take into account the (uniform) thickness of the specimen–25 mm–some constitutive parameters were adapted by multiplying them by this value.

**Table 1.** Values of constitutive parameters used in numerical tests.

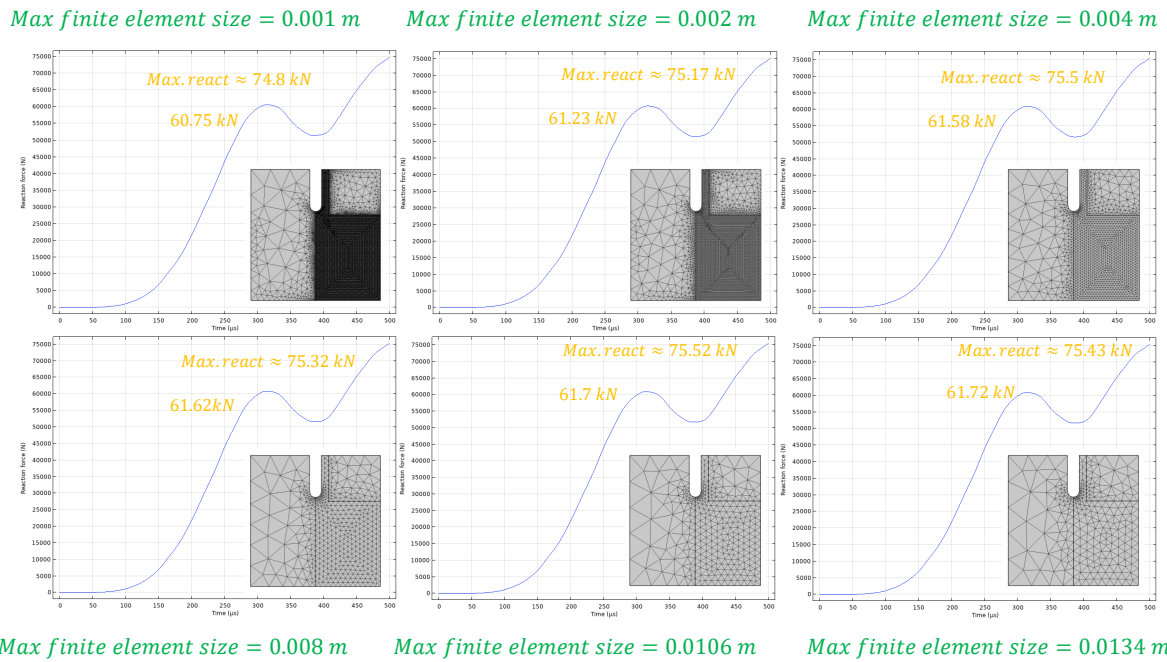| $Y$ | $v$ | $L$ | $\rho$ | $k_\omega$ | $t_f$ | $\triangle t$ | $\gamma$ | $r$ | $m$ |
|---|---|---|---|---|---|---|---|---|---|
| $15\,GPa$ | 0.18 | $0.01118\,m$ | $2400\,kg/m^3$ | $5\,J/m^2$ | $500\,\mu s$ | $0.5\,\mu s$ | 0.0012 | 0.99999 | 0.99999 |

**Figure 3.** Diagrams of the reaction force versus time for different maximum finite element sizes. Data was taken from the convergence analysis performed without implementing the strain gradient regularization.
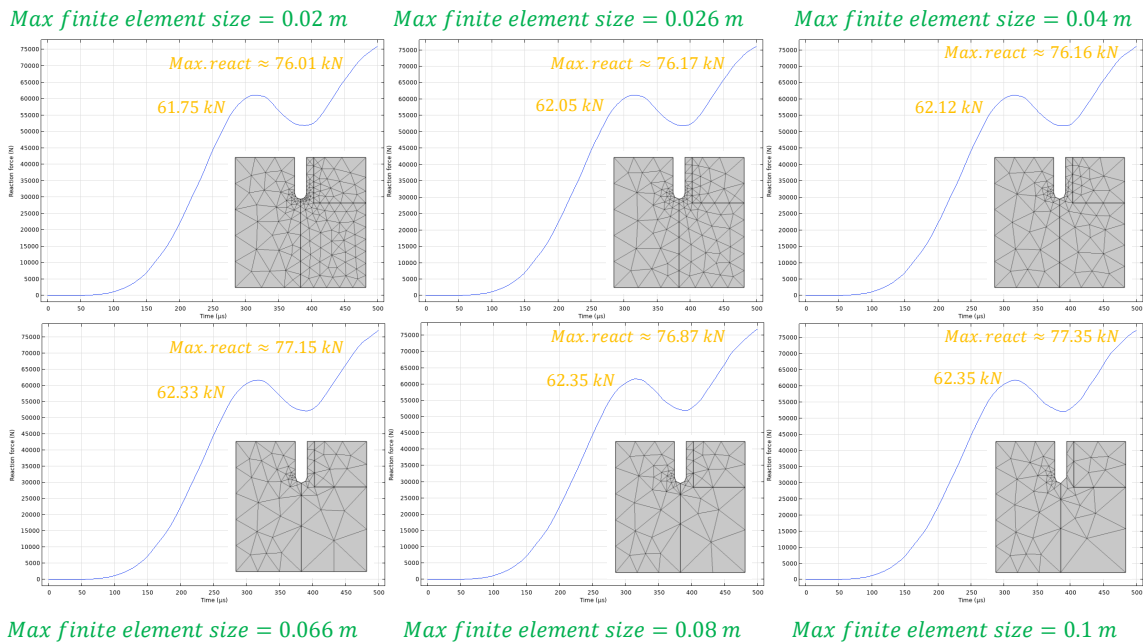


**Figure 4.** Diagrams of the reaction force versus time for different maximum finite element sizes. Data was taken from the convergence analysis performed without implementing the strain gradient regularization.

## 3.2. Convergence analysis

For convergence analysis, we employed two kinds of numerical simulations: elastic and with damage. In the former kind of simulations, to avoid damage and have only an elastic behavior, the threshold on the trace of $G$ was set to 1, an extremely large value, that was never reached in the simulations. In the elastic simulations, it was shown that strain gradient regularization gives better convergence with respect to maximum finite element size (the numbers of degrees of freedom (DOF), and finite elements grow with respect to maximum finite element size). Meanwhile without it, the mesh should be more refined to get the same accuracy.

**Table 2.** Data from convergence analysis without implementation of strain gradient for different mesh sizes.

| DOF | N. of elements | Max. element size, $m$ | Reaction force, $kN$ | Reaction integration over time |
|---|---|---|---|---|
| 656 | 110 | 0.1 | 77.35 | 17.6204 |
| 684 | 115 | 0.08 | 76.87 | 17.5195 |
| 752 | 128 | 0.066 | 77.15 | 17.5876 |
| 796 | 136 | 0.04 | 76.16 | 17.4080 |
| 1108 | 195 | 0.026 | 76.17 | 17.4330 |
| 1614 | 292 | 0.02 | 76.01 | 17.3816 |
| 2768 | 514 | 0.0134 | 75.43 | 17.2840 |
| 3526 | 661 | 0.0106 | 75.52 | 17.3038 |
| 5200 | 987 | 0.008 | 75.32 | 17.2693 |
| 14500 | 2818 | 0.004 | 75.50 | 17.3041 |
| 51046 | 10060 | 0.002 | 75.17 | 17.2411 |
| 186276 | 36991 | 0.001 | 74.80 | 17.1749 |
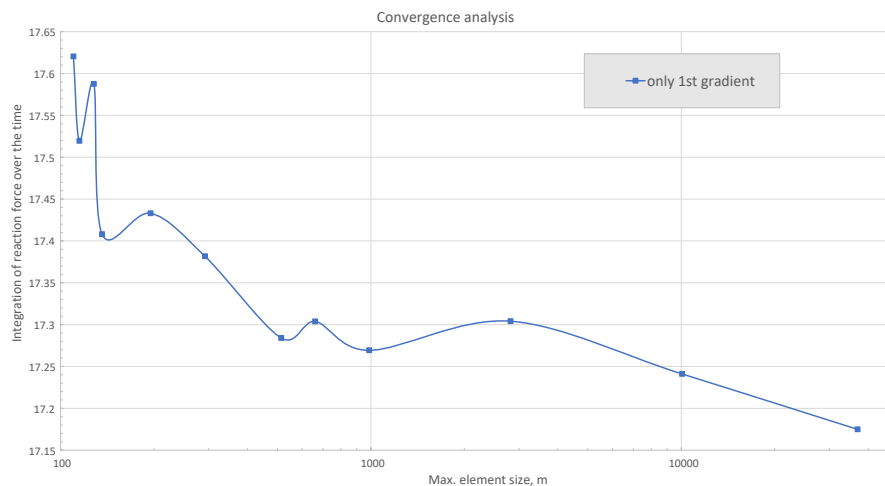


**Figure 5.** Diagram reporting the time integral of the reaction force versus the number of finite elements. Data was taken from the convergence analysis performed without implementing the strain gradient regularization.

*Max finite element size = 0.001 m*   *Max finite element size = 0.002 m*   *Max finite element size = 0.004 m*
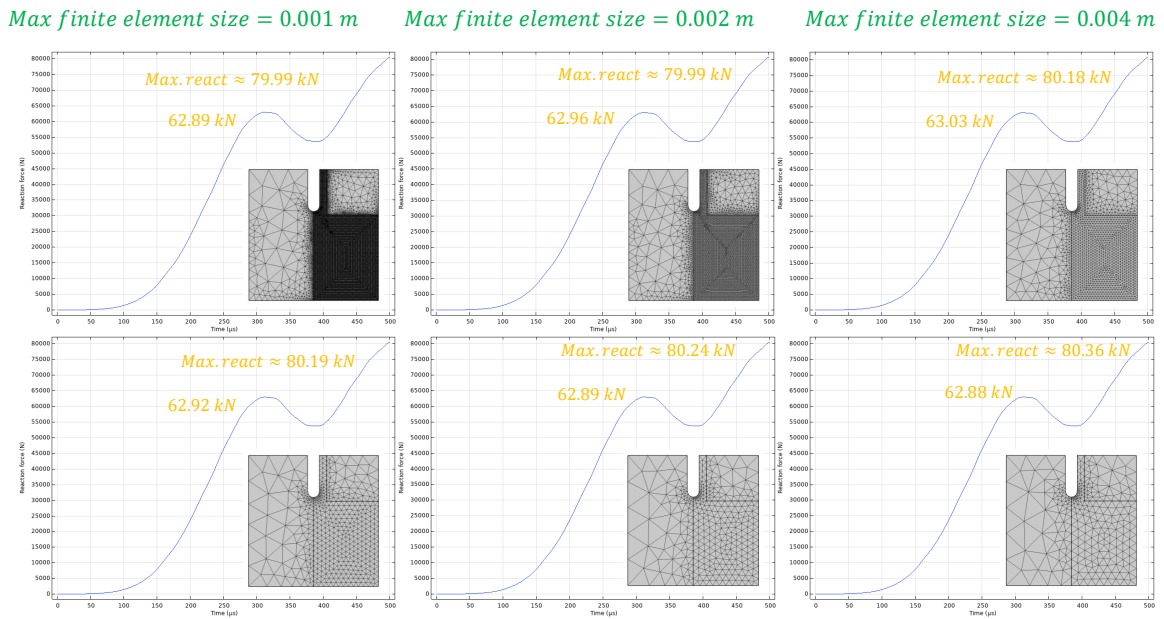


*Max finite element size = 0.008 m*   *Max finite element size = 0.0106 m*   *Max finite element size = 0.0134 m*

**Figure 6.** Diagrams of the reaction force versus time for different maximum finite element sizes. Data was taken from the convergence analysis performed implementing the strain gradient regularization.
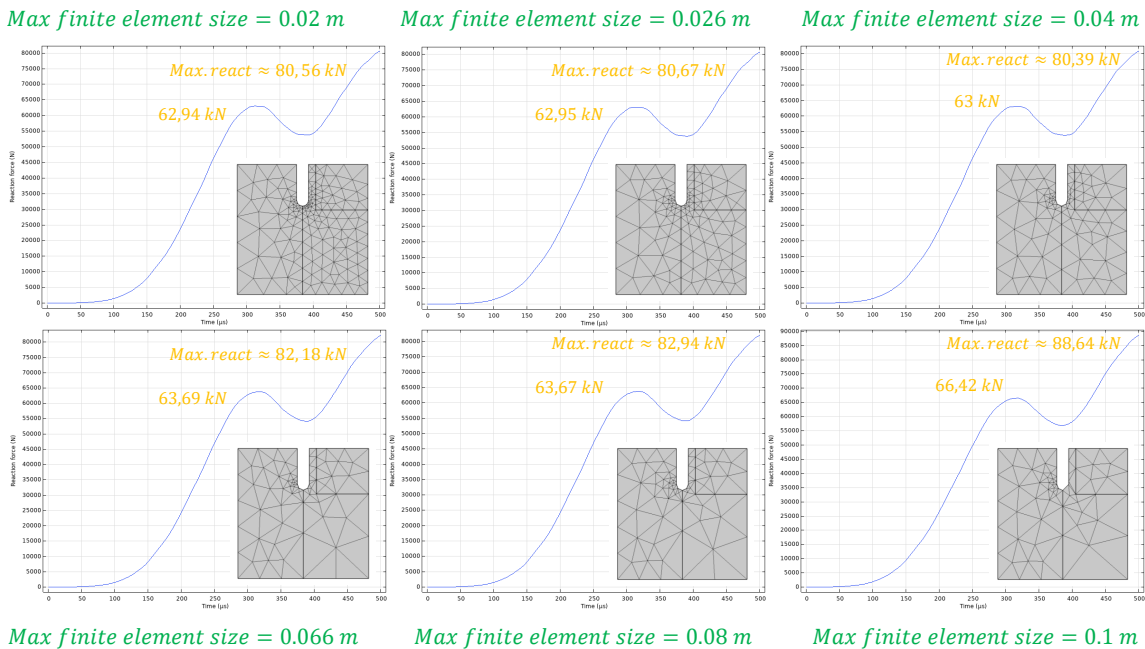
*Max finite element size = 0.02 m*   *Max finite element size = 0.026 m*   *Max finite element size = 0.04 m*



*Max finite element size = 0.066 m*   *Max finite element size = 0.08 m*   *Max finite element size = 0.1 m*

**Figure 7.** Diagrams of the reaction force versus time for different maximum finite element sizes. Data was taken from the convergence analysis performed implementing the strain gradient regularization.

**Table 3.** Data from convergence analysis with implementation of strain gradient for different mesh sizes.

| DOF | N. of elements | Max. element size, $m$ | Reaction force, $kN$ | Reaction integration over time |
|---|---|---|---|---|
| 656 | 110 | 0.1 | 88.64 | 19.5598 |
| 684 | 115 | 0.08 | 88.94 | 18.5620 |
| 752 | 128 | 0.066 | 82.18 | 18.4343 |
| 796 | 136 | 0.04 | 80.39 | 18.1514 |
| 1108 | 195 | 0.026 | 80.67 | 18.2078 |
| 1614 | 292 | 0.02 | 80.56 | 18.1968 |
| 2768 | 514 | 0.0134 | 80.35 | 18.0792 |
| 3526 | 661 | 0.0106 | 80.24 | 18.1218 |
| 5200 | 987 | 0.008 | 80.19 | 18.1218 |
| 14500 | 2818 | 0.004 | 80.18 | 18.1952 |
| 51046 | 10060 | 0.002 | 79.99 | 18.0683 |
| 186276 | 36991 | 0.001 | 79.99 | 18.0746 |
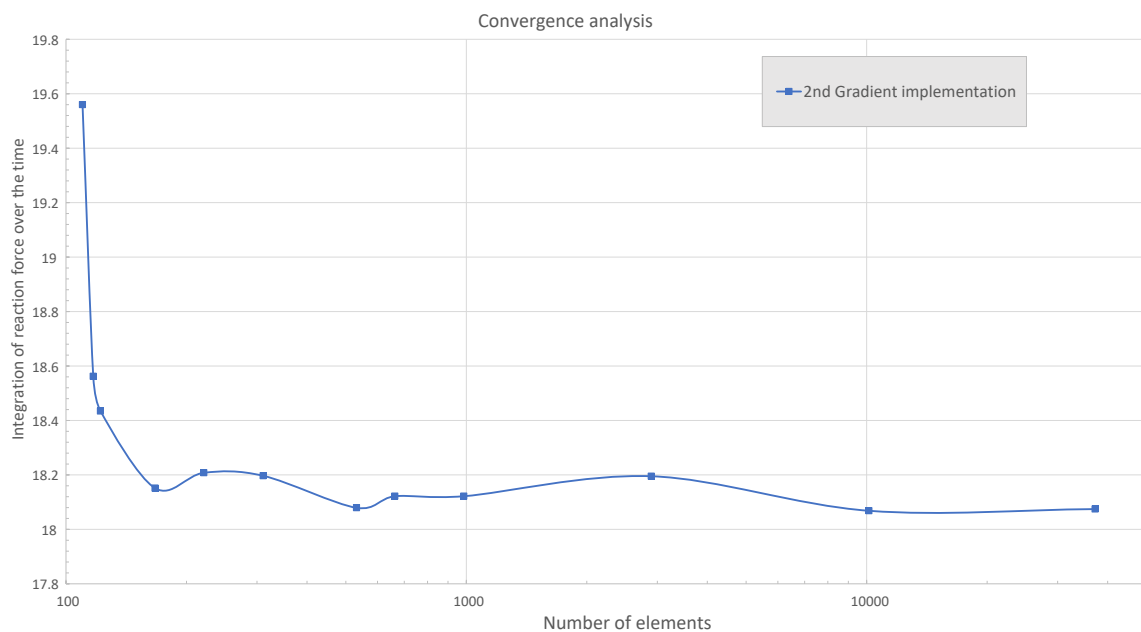


**Figure 8.** Diagram reporting the time integral of the reaction force versus the number of finite elements. Data was taken from the convergence analysis performed implementing the strain gradient regularization.

From Table 2 and Figure 5, we can see that, without implementation of the strain gradient regularization, there is no convergence for the considered values of the maximum finite element size, however the implementation of this term leads us to convergence with refinement of mesh. From Table 3 and Figure 8, we can see that enhanced convergence was achieved making use of the strain gradient regularization, convergence is indeed obtained for maximum finite element size equal to 0.002 m. The same approach to mesh and convergence analysis utilized for the purely elastic case was employed also in the damage

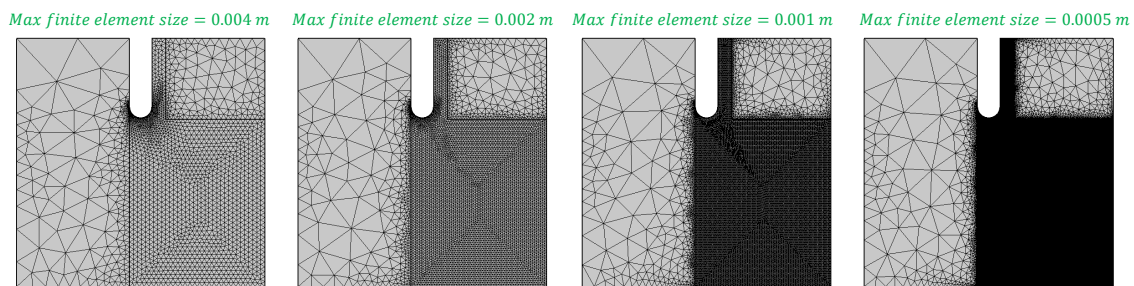case, with applied displacement velocity $v_0 = 3.268$ m/s.



**Figure 9.** Different utilized meshes with indication of the associated maximum element size.
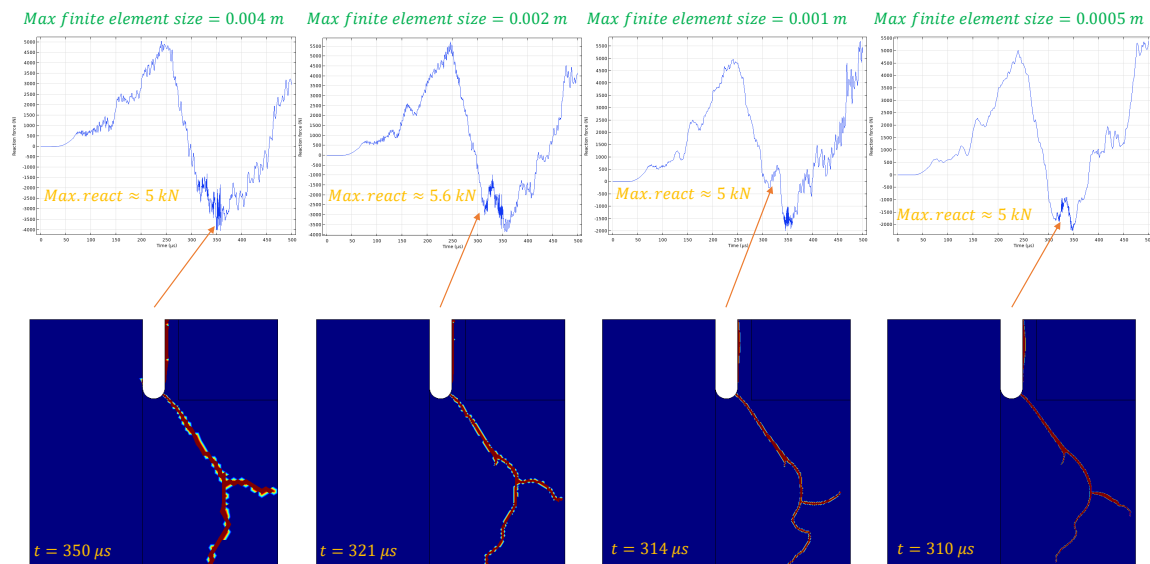


**Figure 10.** Synoptical comparison of reaction force versus time diagrams (first row) and damage contour plots at complete failure (second row) for different maximum finite element sizes.

Figure 9 shows the different utilized meshes, each characterized by a different maximum element size. Figure 10 shows synoptically reaction force versus time diagrams (in the first row) and damage contour plots at complete failure (i.e., the fracture pattern, in the second row) for different maximum finite element sizes. It is seen that the fracture pattern is similar in all cases. Figure 11 compares the fracture thickness for different meshes. For the maximum finite element size equal to 0.004 m, we can see only one damaged element in the crack-transverse direction. However, as the element size decreases, the number of damaged elements in the crack-transverse direction increases. Most importantly, the thickness of the crack is almost the same for all simulations, which leads us to conclude the mesh independence of the results. From Figure 12 we can see that the evolution of the reaction force in time is almost the same for the different considered maximum element sizes, except that it attains its maximum

value at different time instants. Additionally, fracture reaches the specimen's boundary at different times. A maximum mesh size of 0.001 m. was chosen for the simulations that follow in the next subsection.
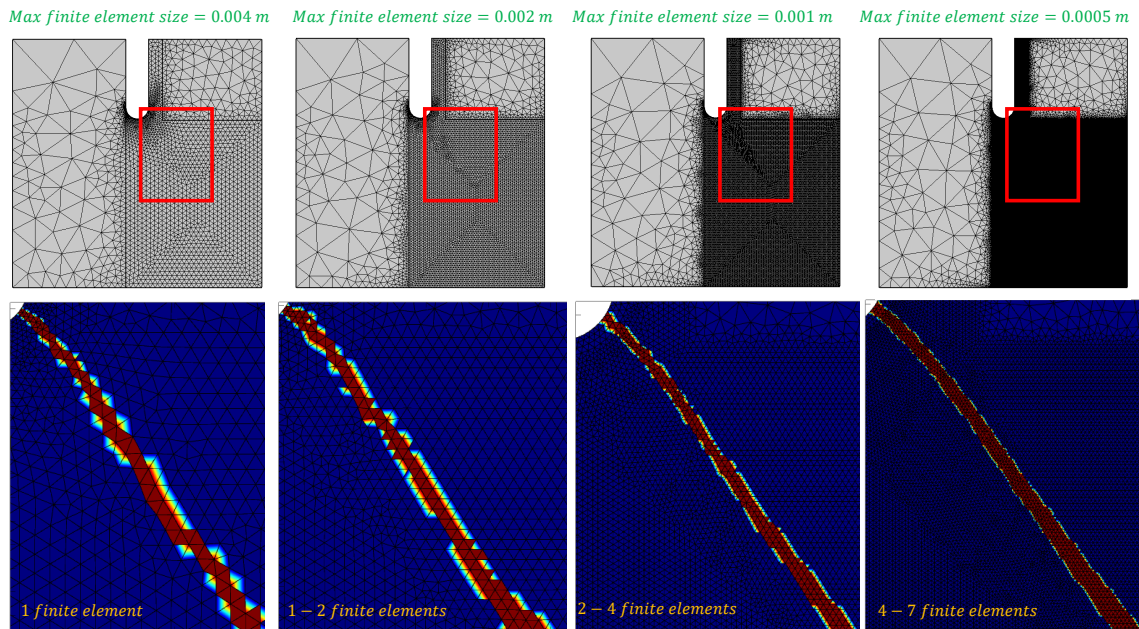


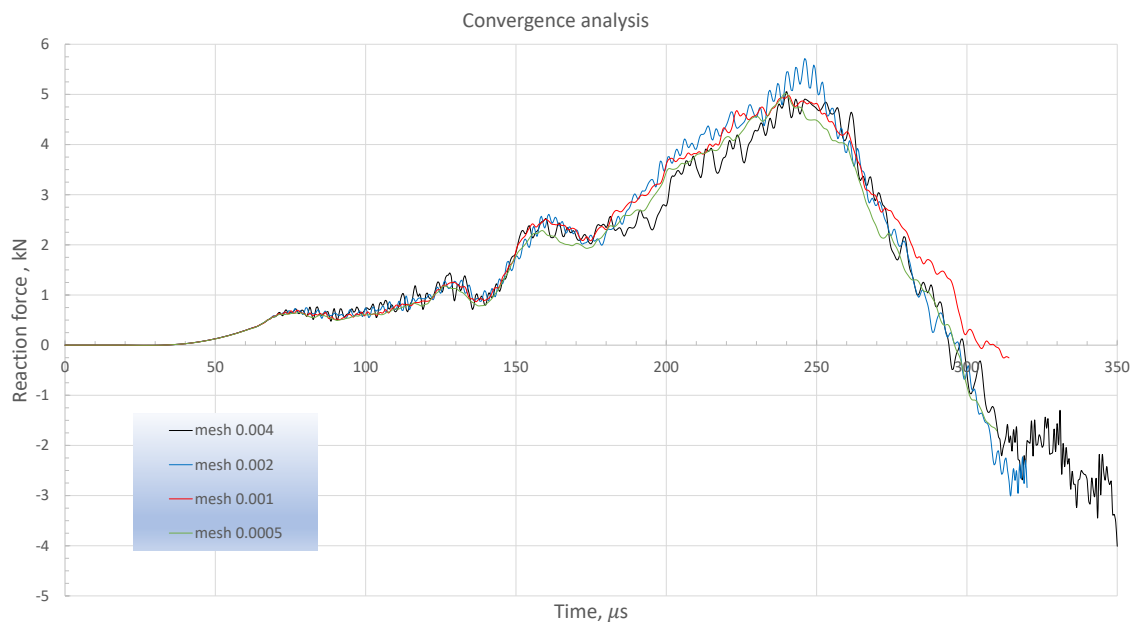**Figure 11.** Comparison of fracture in the specimen's central area for different maximum finite element sizes.



**Figure 12.** Comparison of the reaction force diagram versus time for different maximum finite element sizes.

### 3.3. Numerical results with varying loading rate.

According to the convergence analysis presented above, a set of numerical simulations was performed making use of the same set of constitutive parameters in Table 1 and a mesh with maximum element size equal to 0.001 m. The difference between the different performed simulations lies in the value of the applied displacement velocity. The obtained results were compared with the experimental data.
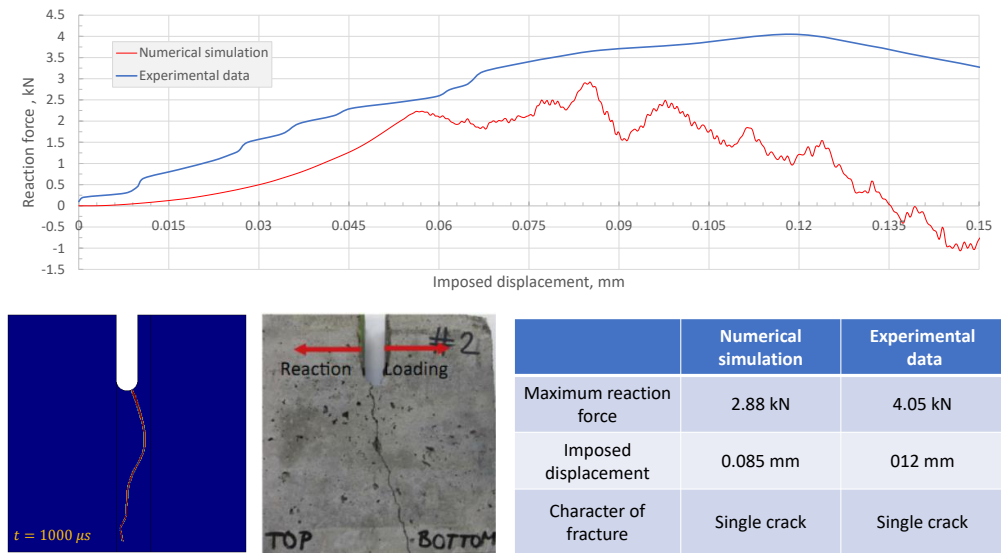


|  | Numerical simulation | Experimental data |
|---|---|---|
| Maximum reaction force | 2.88 kN | 4.05 kN |
| Imposed displacement | 0.085 mm | 012 mm |
| Character of fracture | Single crack | Single crack |

**Figure 13.** Comparison of numerical simulation results with experimental test for applied crack-opening velocity $v_0 = 0.491$ m/s.
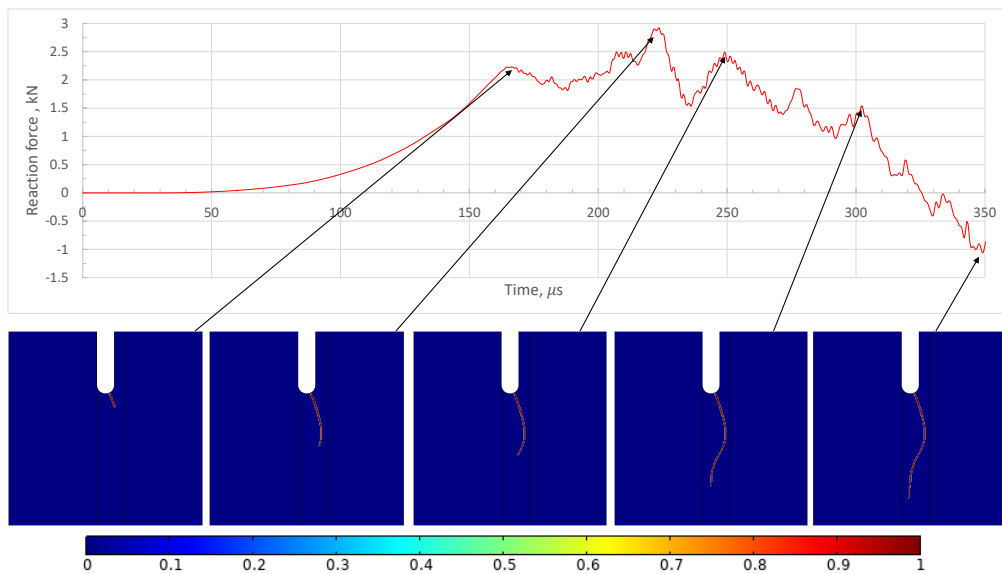


**Figure 14.** Contour plots of damage evolution for applied crack-opening velocity $v_0 = 0.491$ m/s.
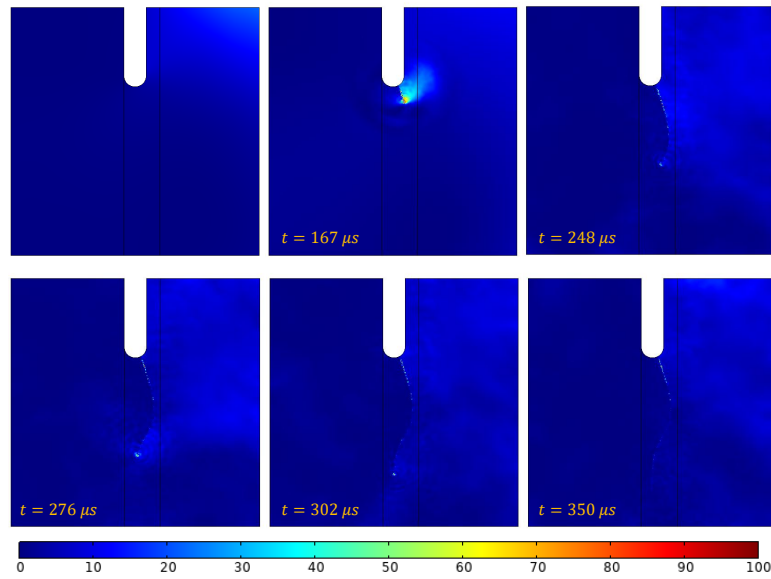
**Figure 15.** Contour plots of kinetic energy density evolution for applied crack-opening velocity $v_0$=0.491 m/s.

Figures 13–15 show, respectively, a comparison of numerical simulation results with experimental ones in terms of reaction force versus imposed displacement diagram and fracture pattern, contour plots of damage evolution, and contour plots of kinetic energy density evolution for applied crack-opening velocity $v_0 = 0.491$ m/s.
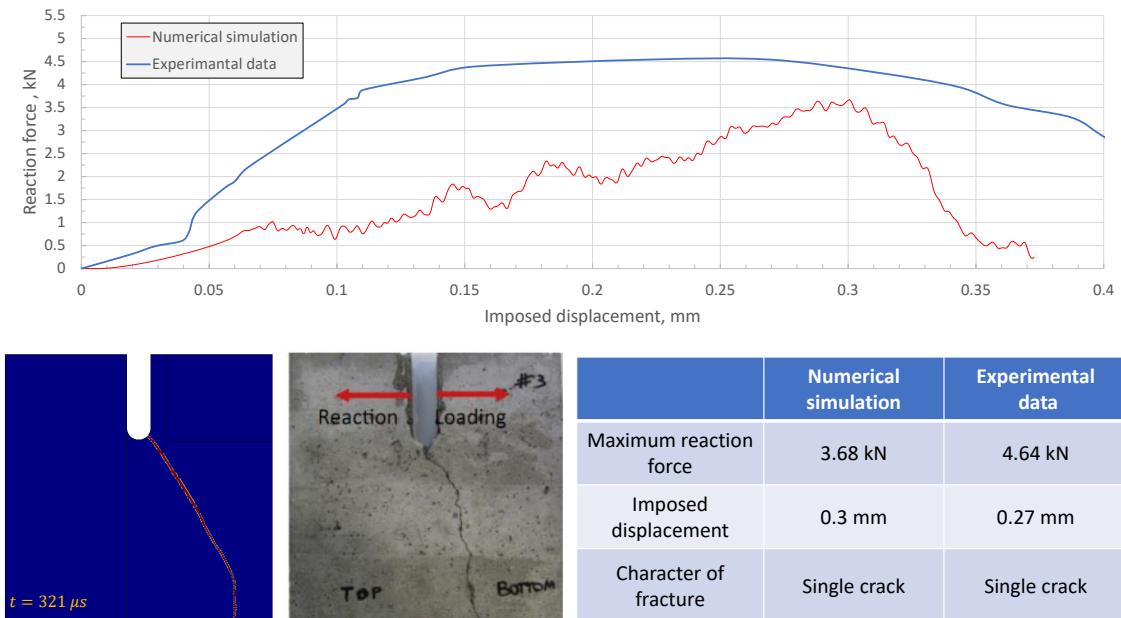


|  | Numerical simulation | Experimental data |
|---|---|---|
| Maximum reaction force | 3.68 kN | 4.64 kN |
| Imposed displacement | 0.3 mm | 0.27 mm |
| Character of fracture | Single crack | Single crack |

**Figure 16.** Comparison of numerical simulation results with experimental test for applied crack-opening velocity $v_0 = 1.375$ m/s.
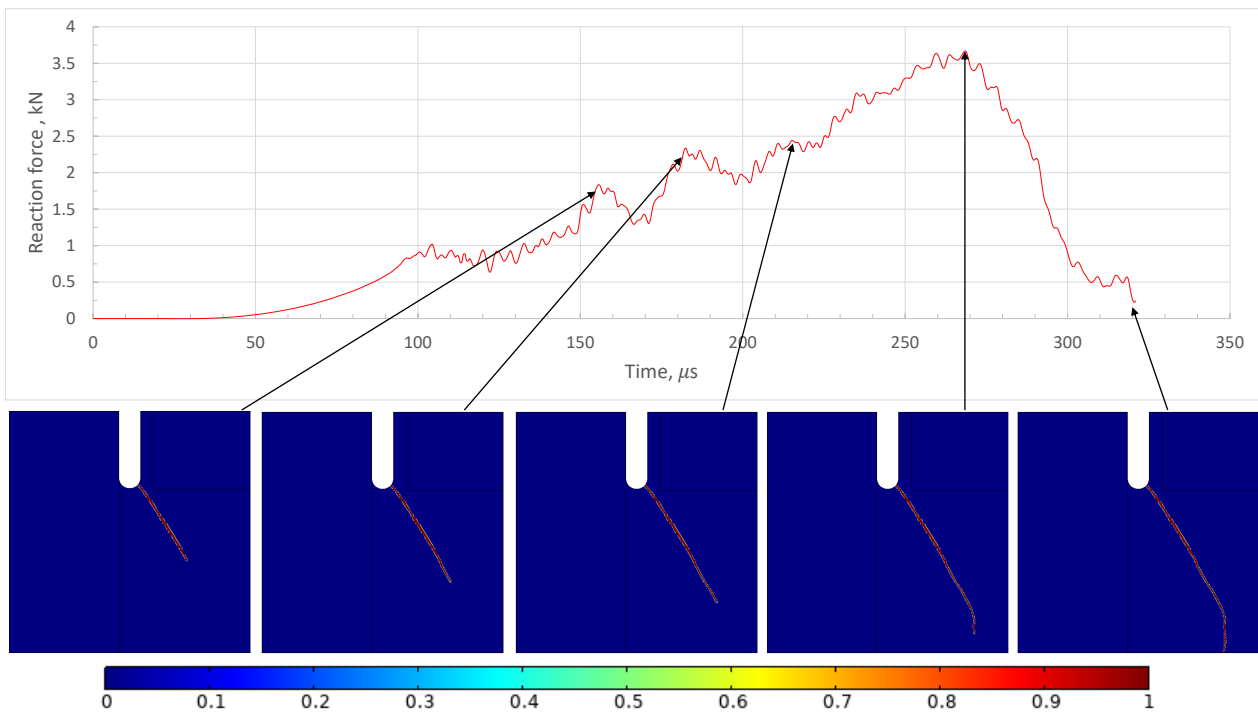
**Figure 17.** Contour plots of damage evolution for applied crack-opening velocity $v_0 = 1.375$ m/s.
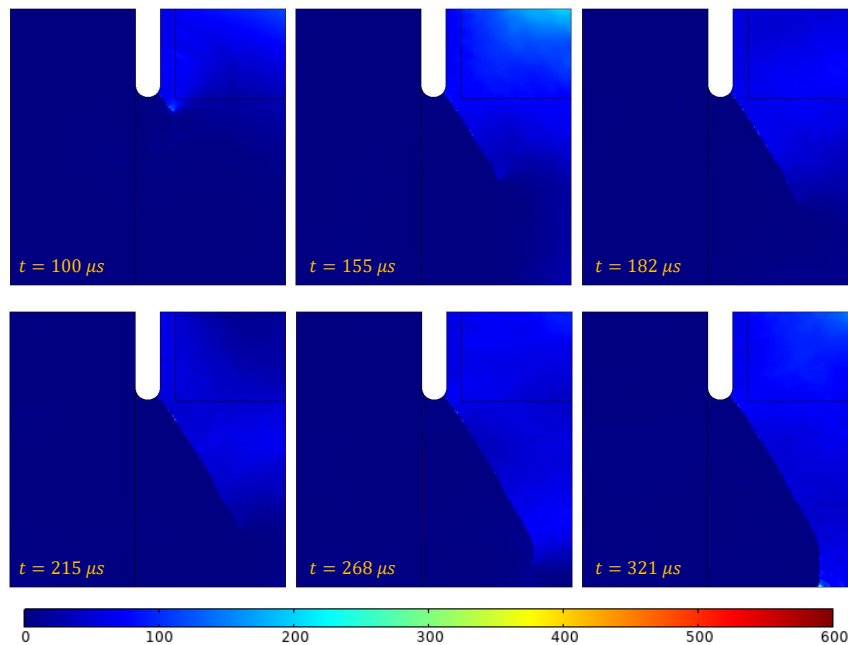


**Figure 18.** Contour plots of kinetic energy density evolution for applied crack-opening velocity $v_0 = 1.375$ m/s.
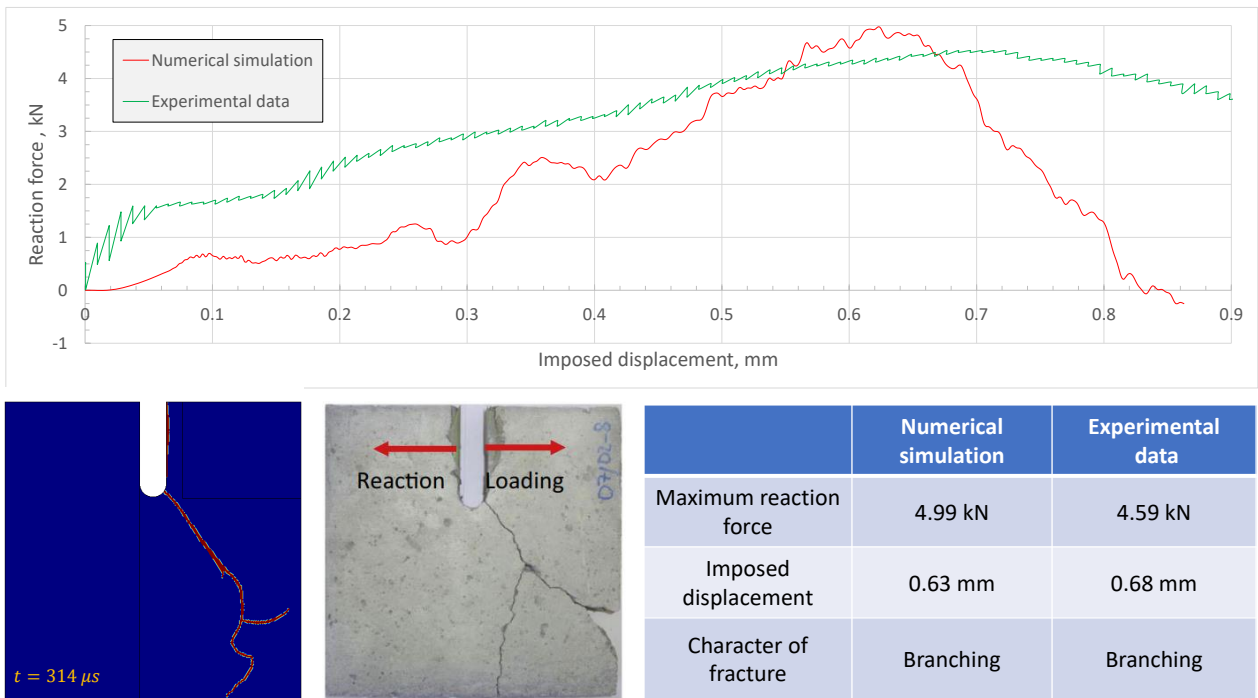
**Figure 19.** Comparison of numerical simulation results with experimental test for applied crack-opening velocity $v_0 = 3.268$ m/s.
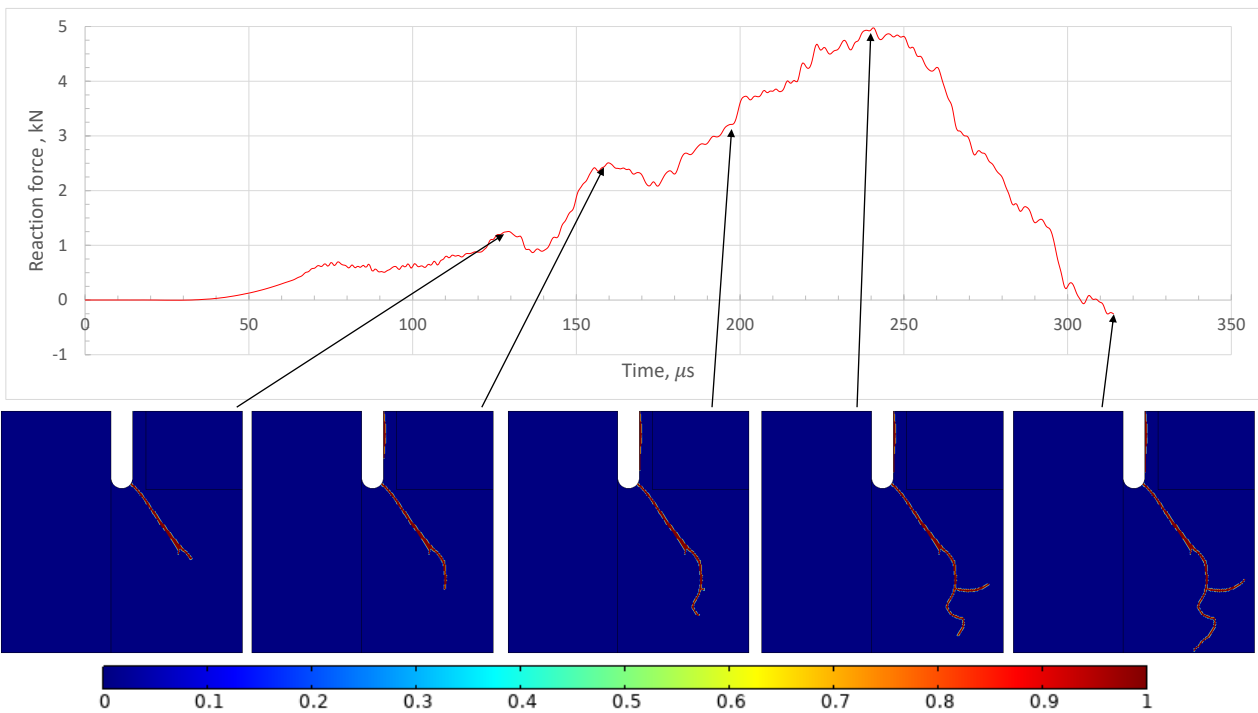


**Figure 20.** Contour plots of damage evolution for applied crack-opening velocity $v_0 = 3.268$ m/s.
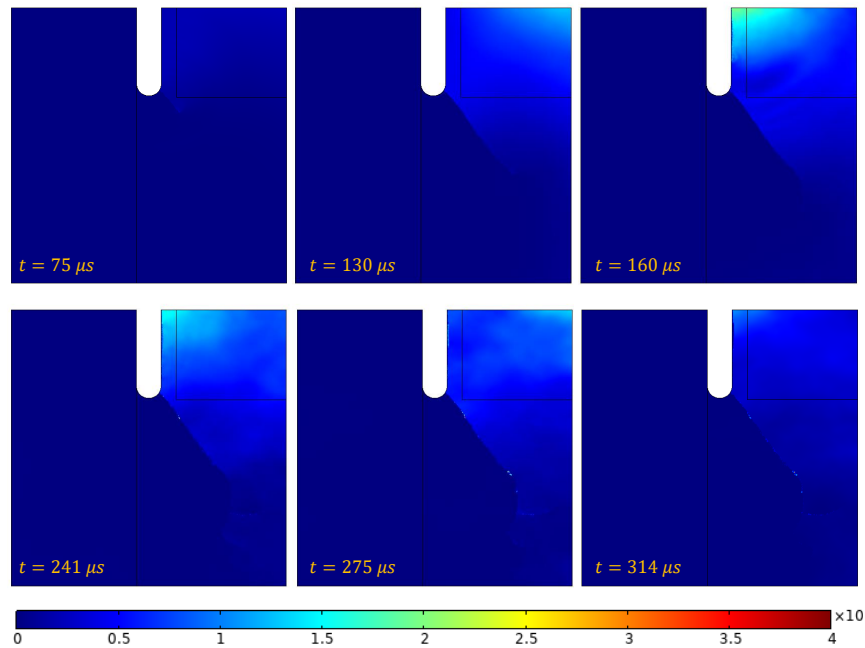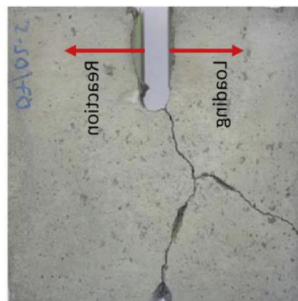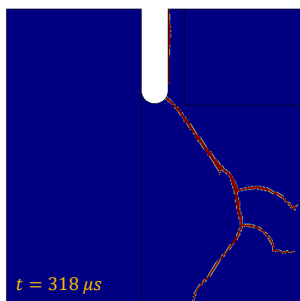
**Figure 21.** Contour plots of kinetic energy density evolution for applied crack-opening velocity $v_0 = 3.268$ m/s.



| | Numerical simulation | Experimental data |
|---|---|---|
| Maximum reaction force | 5.00 kN | 5.66 kN |
| Imposed displacement | 0.85 mm | 0.99 mm |
| Character of fracture | Multiple branching | Branching |

**Figure 22.** Comparison of numerical simulation results with experimental test for applied crack-opening velocity $v_0 = 4.298$ m/s.

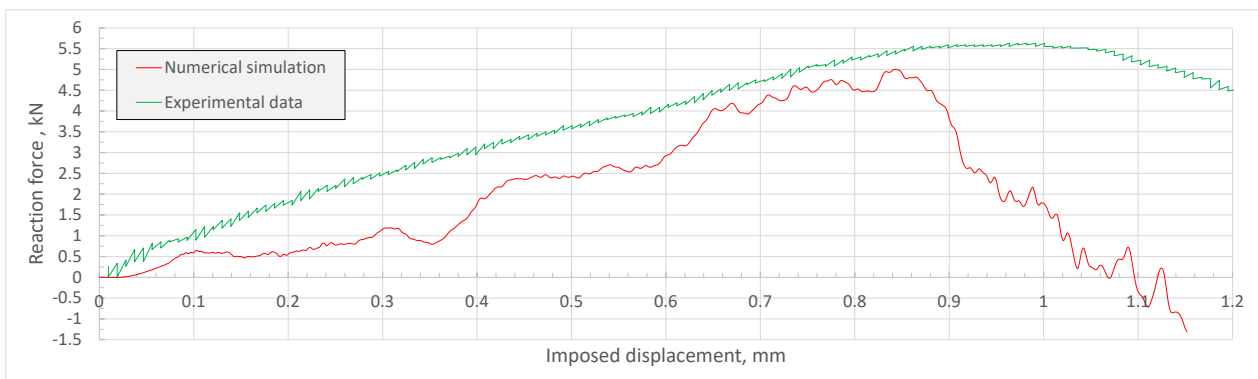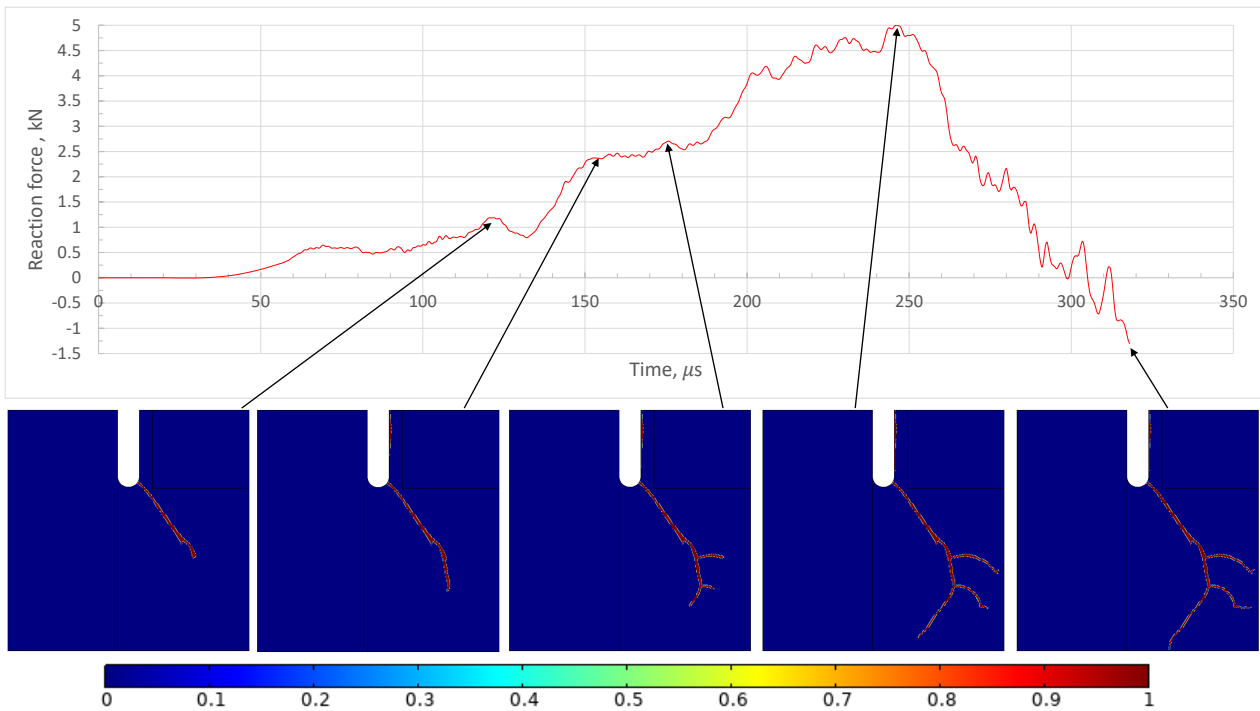**Figure 23.** Contour plots of damage evolution for applied crack-opening velocity $v_0 = 4.298$ m/s.
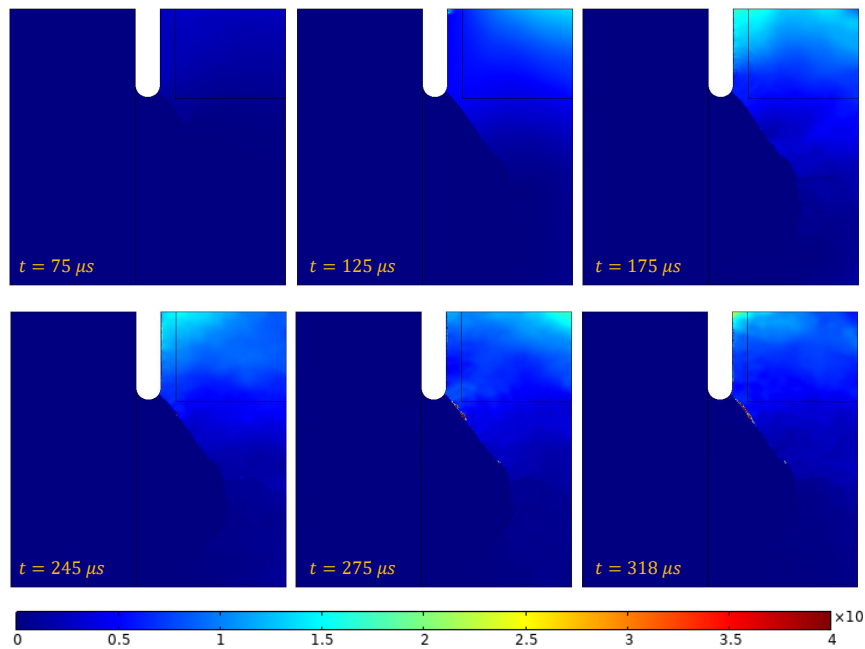


**Figure 24.** Contour plots of kinetic energy density evolution for applied crack-opening velocity $v_0 = 4.298$ m/s.
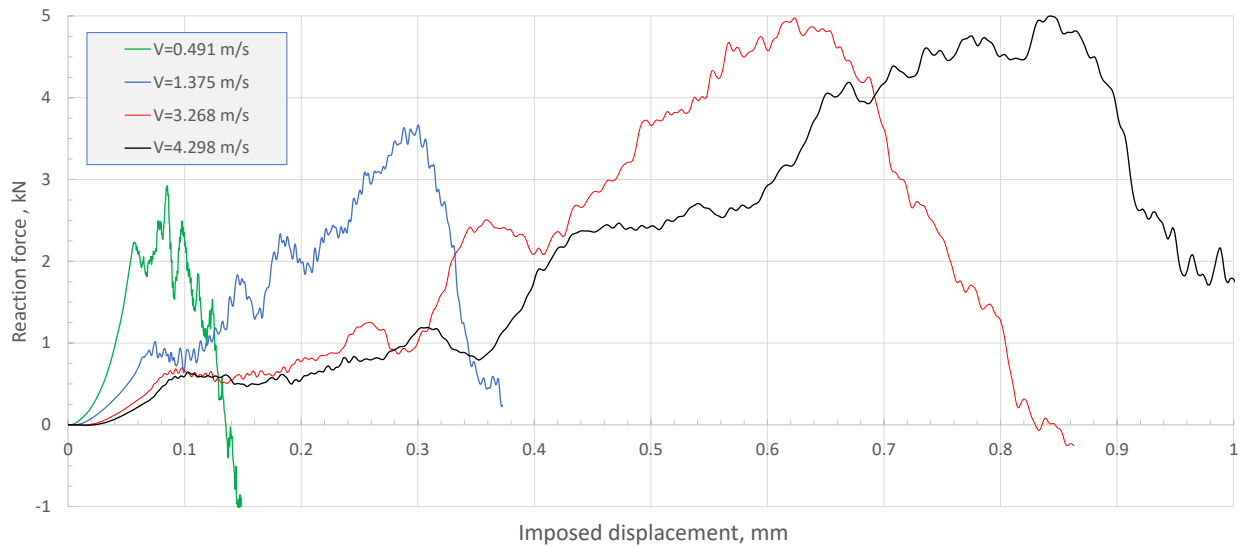
**Figure 25.** Comparison of reaction force versus imposed displacement diagrams computed for different loading rates.
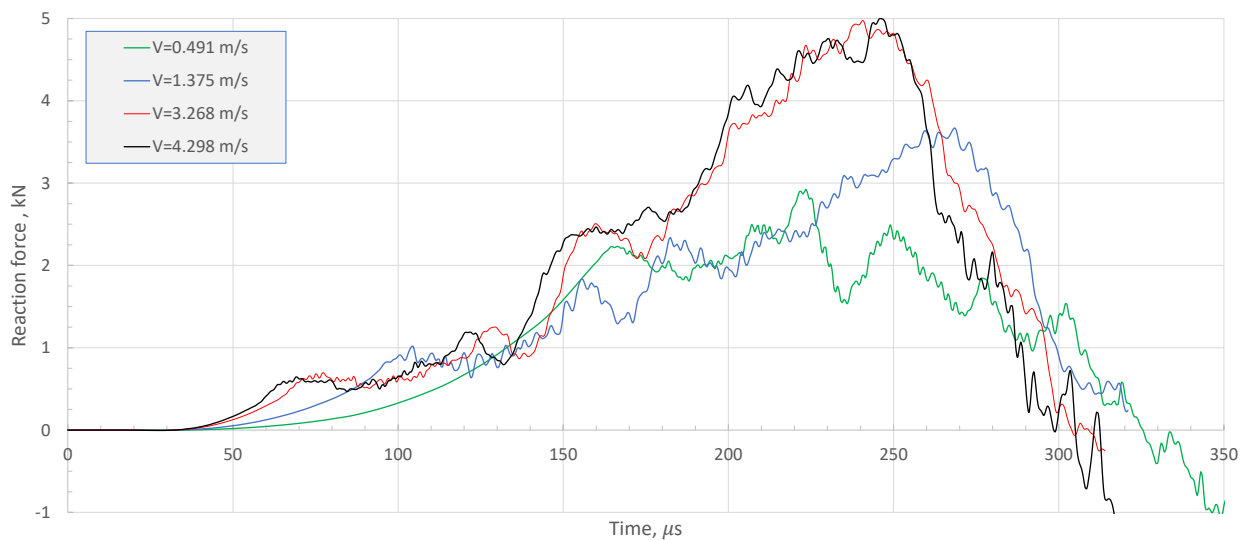


**Figure 26.** Comparison of reaction force versus imposed time diagrams computed for different loading rates.

Figures 16 –18 are analogous but refer to an applied crack-opening velocity $v_0 = 1.375$ m/s, while Figures 19–21 and Figures 22–24 do refer to an applied crack-opening velocity $v_0 = 3.268$ m/s and $v_0 = 4.298$ m/s, respectively. It is possible to observe that the path and character of the fracture match the experimental data, except for the higher loading rate. The reaction force versus imposed displacement diagram properties match relatively well, too. Furthermore, we observe that, for low loading rate, the propagation is almost vertical, leading to standard mode-I crack propagation, while for increasing crack-opening velocity the fracture deviates from the vertical direction and branching phenomena are observed. For the applied crack-opening velocity $v_0 = 1.375$ m/s, the computed kink angle is the

same as in the experimental data. However, at the end of the fracture process, the computed fracture touches a different point of the boundary. For the applied crack-opening velocity $v_0 = 3.375$ m/s, one can see simple branching, while for the applied crack-opening velocity $v_0 = 4.298$ m/s, we can see multiple branching. With this difference, we can explain that it does not correspond that all twelve experimental specimens were done from the same concrete and have exactly the same properties. As well, it is not enough that the statistics and some errors could occur during the experiments. Anyway numerical simulations are the way to predict the behavior and it could be improved. Table 4 reports synoptically, for comparison, the reaction force measured experimentally and computed with various approaches–including the one presented in this paper–for different applied velocities.

**Table 4.** Reaction force measured experimentally and computed with various approaches–including the one presented in this paper–for different applied velocities. Results are reported in kN.

| Applied $v_0$ (m/s) | Exp. results [41] | Numerical results obtained with various approaches by | | | | | | |
|---|---|---|---|---|---|---|---|---|
| | | Ozbolt [42] | This paper | Hai [22] | Wu's IH-PD [71] | Wu's FH-PD [71] | Bui [5] | Qinami [55] |
| 0.491 | 4.05 | 4.12 | 2.88 | - | - | - | - | - |
| 1.375 | 4.64 | 3.54 | 3.68 | 3.75 | ≈ 4.3 | ≈ 5.5 | ≈ 3.3 | ≈ 4.7 |
| 3.268 | 4.59 | 4.76 | 4.99 | 4.70 | ≈ 4.6 | ≈ 6.1 | ≈ 3.3 | ≈ 6.1 |
| 4.298 | 5.66 | 5.15 | 5.00 | - | ≈ 5.6 | ≈ 6.1 | - | ≈ 6.5 |

## 4. Conclusions

In this paper, we have focused on the loading rate effect on fracture propagation in brittle materials with strain gradient effects. We have demonstrated that, the slower the applied loading velocity, the less the maximum reaction force; and the faster the applied loading velocity, the higher must be the imposed displacement to reach the maximum value of the reaction force; cfr. Figure 25. It is also observed that the nonsymmetric increasing loading rate leads to a deviation from standard mode-I crack propagation consisting of crack deviation and simple and multiple branching that cannot be revealed in the quasi-static case. It is worth it to note that, as expected, kinetic energy concentrates in the specimen's region, directly putting in movement by the loading and by the occurrence of fracture, which allows crack opening and, hence, movement of the body particles in that region. Increasing the applied loading velocity, one can also see the growth of some orders of magnitude of the kinetic energy, which suggests that this is the key quantity underlying the loading rate dependent behavior of fracture propagation.

## Author contributions

L.P, A.M. and E.B. conceived the presented idea and verified the analytical methods. V.M., L.P, A.M., D.T. and E.B developed the theory. V.M., L.P, F.J.L.T., A.M., D.T., F.F. and E.B discussed the theoretical model. V.M., D.T. and E.B performed the computations. V.M., L.P, F.J.L.T., C.D.S., A.M., D.T. and E.B discussed the numerical results. All authors contributed to the final manuscript.

**Use of AI tools declaration**

The Authors declare they have not used Artificial Intelligence (AI) tools in the creation of this article.

**Acknowledgments**

**Conflict of interest**

The Authors declare that there is no conflict of interest.

**References**

1. B. E. Abali, W. H. Müller, F. dell'Isola, Theory and computation of higher gradient elasticity theories based on action principles, *Arch. Appl. Mech.*, **87** (2017), 1495–1510. https://doi.org/10.1007/s00419-017-1266-5

2. J. J. Alibert, P. Seppecher, F. Dell'Isola, Truss modular beams with deformation energy depending on higher displacement gradients, *Math Mech Solids*, **8** (2003), 51–73. https://doi.org/10.1177/1081286503008001658

3. G. Aydin, B. C. Sarar, M. E. Yildizdag, B. E. Abali, Investigating infill density and pattern effects in additive manufacturing by characterizing metamaterials along the strain-gradient theory, *Math Mech Solids*, **27** (2022), 2002–2016. https://doi.org/10.1177/10812865221100978

4. E. Barchiesi, A. Misra, L. Placidi, E. Turco, Granular micromechanics-based identification of isotropic strain gradient parameters for elastic geometrically nonlinear deformations, *Z Angew Math Mech*, **101** (2021), e202100059.

5. T. Q. Bui, H. Tran, X. Hu, C. T. Wu, Simulation of dynamic brittle and quasi-brittle fracture: a revisited local damage approach, *Int J Fracture*, **236** (2022), 59–85.

6. E. Cadoni, A. Caverzani, M. di Priscoi, Dynamic behaviour of hpfrcc in tension, *EPJ Web of Conferences*, **26** (2012), 01014. https://doi.org/10.1051/epjconf/20122601014

7. C. H. Chen, E. Bouchbinder, A. Karma, Instability in dynamic fracture and the failure of the classical theory of cracks, *Nat. Phys.*, **13** (2017), 1186–1190. https://doi.org/10.1038/nphys4237

8. Y. Cui, X. Zeng, V. B. C. Tan, Z. Zhang, Experimental and numerical studies of niti dynamic fracture behaviors under the impact loading, *Int. J. Mech. Sci.*, **235** (2022), 107724. https://doi.org/10.1016/j.ijmecsci.2022.107724

9. H. Darban, R. Luciano, A. Caporale, F. Fabbrocino, Higher modes of buckling in shear deformable nanobeams, *Int J Eng Sci*, **154** (2020), 103338. https://doi.org/10.1016/j.ijengsci.2020.103338

10. F. dell'Isola, L. Placidi, *Variational principles are a powerful tool also for formulating field theories*, In: F. dell'Isola, S. Gavrilyuk, (eds) Variational Models and Methods in Solid and Fluid Mechanics. Vienna: Springer, **535** (2001), 1–15. https://doi.org/10.1007/978-3-7091-0983-0_1

11. F. dell'Isola, U. Andreaus, L. Placidi, At the origins and in the vanguard of peridynamics, non-local and higher-gradient continuum mechanics: An underestimated and still topical contribution of gabrio piola, *Math Mech Solids*, **20** (2015), 887–928. https://doi.org/10.1177/1081286513509811

12. F. dell'Isola, R. Fedele, Irreducible representation of surface distributions and Piola transformation of external loads sustainable by third gradient continua, *Comptes Rendus. Mécanique*, **351** (2023), 1–30.

13. F. dell'Isola, P. Seppecher, A. Madeo, How contact interactions may depend on the shape of cauchy cuts in nth gradient continua: approach "à la d'alembert", *Z. Angew. Math. Phys.*, **63** (2012), 1119–1141. https://doi.org/10.1007/s00033-012-0197-9

14. V. A. Eremeyev, F. dell'Isola, On weak solutions of the boundary value problem within linear dilatational strain gradient elasticity for polyhedral lipschitz domains, *Math Mech Solids*, **27** (2022), 433–445. https://doi.org/10.1177/10812865211025576

15. V. A. Eremeyev, S. A. Lurie, Y. O. Solyaev, F. dell'Isola, On the well posedness of static boundary value problem within the linear dilatational strain gradient elasticity, *Z. Angew. Math. Phys.*, **71** (2020), 182. https://doi.org/10.1007/s00033-020-01395-5

16. A. C. Eringen, *Microcontinuum Field Theories I: Foundations and Solids*, New York: Springer-Verlang, 1999.

17. O. Essersi, M. Tarfaoui, S. Boyd, R. Shenoi, F. Meraghni, Experimental study of dynamic behaviour of aluminum/aluminum and composite/composite double lap joints, *Appl Mech Mater*, **62** (2011), 155–163. https://doi.org/10.4028/www.scientific.net/AMM.62.155

18. F. Fabbrocino, M. F. Funari, F. Greco, P. Lonetti, R. Luciano, R. Penna, Dynamic crack growth based on moving mesh method, *Compos. B. Eng.*, **174** (2019), 107053. https://doi.org/10.1016/j.compositesb.2019.107053

19. M. F. Funari, S. Spadea, F. Fabbrocino, R. Luciano, A moving interface finite element formulation to predict dynamic edge debonding in frp-strengthened concrete beams in service conditions, *Fibers*, **8** (2020), 42. https://doi.org/10.3390/fib8060042

20. F. Galvez, D. Cendon, N. Garcia, A. Enfedaque, V. Sanchez-Galvez, Dynamic fracture toughness of a high strength armor steel, *Eng Fail Anal*, **16** (2009), 2567–2575. https://doi.org/10.1016/j.engfailanal.2009.04.020

21. P. Germain, The method of virtual power in continuum mechanics. Part 2: Microstructure, *SIAM J Appl Math*, **25** (1973), 556–575. https://doi.org/10.1137/0125053

22. L. Hai, J. Li, A rate-dependent phase-field framework for the dynamic failure of quasi-brittle materials, *Eng. Fract. Mech.*, **252** (2021), 107847. https://doi.org/10.1016/j.engfracmech.2021.107847

23. R. H. Cao, R. Yao, T. Hu, C. Wang, K. Li, J. Meng, Failure and mechanical behavior of transversely isotropic rock under compression-shear tests: Laboratory testing and numerical simulation, *Eng. Fract. Mech.*, **241** (2021), 107389. https://doi.org/10.1016/j.engfracmech.2020.107389

24. X. Huang, A. R. Tabkhi, V. Sadeghian, O. S. Kwon, Impact of loading rate during hybrid simulation on seismic response of steel structures, *Earthq Eng Struct Dyn*, **51** (2022), 2813–2836. https://doi.org/10.1002/eqe.3703

25. H. H. Jama, G. N. Nurick, M. R. Bambach, R. H. Grzebieta, X. L. Zhao, Steel square hollow sections subjected to transverse blast loads, *Thin Wall Struct*, **53** (2012), 109–122. https://doi.org/10.1016/j.tws.2012.01.007

26. K. Khaled, G. Mohamed, Modelling of the influence of tensile test speed on the fracture load, *ASM Sci. J.*, **12** (2019), 1–12.

27. Q. Li, X. Jiang, T. Zeng, S. Xu, Experimental investigation on strain rate effect of high-performance fiber reinforced cementitious composites subject to dynamic direct tensile loading, *Cement Concrete Res*, **157** (2022), 106825. https://doi.org/10.1016/j.cemconres.2022.106825

28. X. Liu, P. Yu, B. Zheng, E. Oterkus, X. He, C. Lu, Prediction of graphene's mechanical and fracture properties via peridynamics, *Int. J. Mech. Sci.*, **266** (2024), 108914. https://doi.org/10.1016/j.ijmecsci.2023.108914

29. R. Luciano, H. Darban, C. Bartolomeo, F. Fabbrocino, D. Scorza, Free flexural vibrations of nanobeams with non-classical boundary conditions using stress-driven nonlocal model, *Mech Res Commun*, **107** (2020), 103536. https://doi.org/10.1016/j.mechrescom.2020.103536

30. K. K. Mahato, M. Biswal, D. K. Rathore, R. K. Prusty, K. Dutta, B. C. Ray, Effect of loading rate on tensile properties and failure behavior of glass fibre/epoxy composite, *IOP Conference Series: Materials Science and Engineering*, **115** (2016), 012017. https://dx.doi.org/10.1088/1757-899X/115/1/012017

31. G. Mancusi, F. Fabbrocino, L. Feo, F. Fraternali, Size effect and dynamic properties of 2d lattice materials, *Compos. B. Eng.*, **112** (2017), 235–242. https://doi.org/10.1016/j.compositesb.2016.12.026

32. J. Marigo, Modelling of brittle and fatigue damage for elastic material by growth of microvoids, *Eng. Fract. Mech.*, **21** (1985), 861–874. https://doi.org/10.1016/0013-7944(85)90093-1

33. V. Mentl, J. Dzugan, Impact compression and tensile testing by means of a charpy pendulum, in *WIT Transactions on The Built Environment*, Ashurst: WIT Press, 2008, 55–61.

34. R. D. Mindlin, Micro-structure in linear elasticity, *Arch Ration Mech Anal*, **16** (1964), 51–78. https://doi.org/10.1007/BF00248490

35. A. Misra, P. Luca, E. Turco, *Variational Methods for Discrete Models of Granular Materials*, In: H. Altenbach, A. Öchsner, (eds) Encyclopedia of Continuum Mechanics, Berlin: Springer-Verlag, 2020. https://doi.org/10.1007/978-3-662-55771-6_172

36. A. Misra, L. Placidi, F. dell'Isola, E. Barchiesi, Identification of a geometrically nonlinear micromorphic continuum via granular micromechanics, *Z. Angew. Math. Phys.*, **72** (2021), 157. https://doi.org/10.1007/s00033-021-01587-7

37. N. Nejadsadeghi, A. Misra, Extended granular micromechanics approach: a micromorphic theory of degree n, *Math Mech Solids*, **25** (2020), 407–429. https://doi.org/10.1177/1081286519879479

38. H. Nguyen, W. Li, Z. P. Bažant, Y. Bazilevs, Isogeometric smooth crack-band model (isCBM) using spress-sprain relations adapted to microplane theory, *J Mech Phys Solids*, **181** (2023), 105470. https://doi.org/10.1016/j.jmps.2023.105470

39. Z. Nowak, Z. L. Kowalewski, T. Szymczak, Low velocity perforation of thick magnesium alloy AM60 plates impacted by rigid conical-nose impactor, *Arch. Civ. Mech. Eng.*, **23** (2022), 5. https://doi.org/10.1007/s43452-022-00525-2

40. J. Ožbolt, K. K. Rah, D. Meštrović, Influence of loading rate on concrete cone failure, *Int J Fract*, **139** (2006), 239–252. https://doi.org/10.1007/s10704-006-0041-3

41. J. Ožbolt, J. Bošnjak, E. Sola, Dynamic fracture of concrete compact tension specimen: Experimental and numerical study, *Int J Solids Struct*, **50** (2013), 4270–4278. https://doi.org/10.1016/j.ijsolstr.2013.08.030

42. J. Ožbolt, A. Sharma, H. W. Reinhardt, Dynamic fracture of concrete–compact tension specimen, *Int J Solids Struct*, **48** (2011), 1534–1543. https://doi.org/10.1016/j.ijsolstr.2011.01.033

43. B. Paermentier, S. Cooreman, P. Verleysen, S. Chandran, S. Coppieters, R. Talemi, A dynamic tensile tear test methodology to characterise dynamic fracture behaviour of modern high-grade pipeline steels, *Eng. Fract. Mech.*, **272** (2022), 108687. https://doi.org/10.1016/j.engfracmech.2022.108687

44. A. K. Pandouria, S. Kumar and V. Tiwari, Experimental study of dynamic fracture behavior of Al7075-T651 under different loading rates, *Mater. Today Commun.*, **33** (2022), 104529. https://doi.org/10.1016/j.mtcomm.2022.104529

45. S. Patnaik, F. Semperlotti, Variable-order fracture mechanics and its application to dynamic fracture, *NPJ Comput. Mater.*, **7** (2021), 27. https://doi.org/10.1038/s41524-021-00492-x

46. L. Placidi, U. Andreaus, A. Della Corte, T. Lekszycki, Gedanken experiments for the determination of two-dimensional linear second gradient elasticity coefficients, *Z. Angew. Math. Phys.*, **66** (2015), 3699–3725. https://doi.org/10.1007/s00033-015-0588-9

47. L. Placidi, F. dell'Isola, N. Ianiro, G. Sciarra, Variational formulation of pre-stressed solid–fluid mixture theory, with an application to wave phenomena, *Eur J Mech-A/Solid*, **27** (2008), 582–606. https://doi.org/10.1016/j.euromechsol.2007.10.003

48. L. Placidi, A variational approach for a nonlinear 1-dimensional second gradient continuum damage model, *Contin. Mech. Thermodyn.*, **27** (2015), 623–638. https://doi.org/10.1007/s00161-014-0338-9

49. L. Placidi, A variational approach for a nonlinear one-dimensional damage-elasto-plastic second-gradient continuum model, *Contin. Mech. Thermodyn.*, **28** (2016), 119–137. https://doi.org/10.1007/s00161-014-0405-2

50. L. Placidi, E. Barchiesi, Energy approach to brittle fracture in strain-gradient modelling, *Proc. Math. Phys. Eng. Sci.*, **474** (2018), 20170878. https://doi.org/10.1098/rspa.2017.0878

51. L. Placidi, E. Barchiesi, A. Misra, A strain gradient variational approach to damage: a comparison with damage gradient models and numerical results, *Math. Mech. Complex Syst.*, **6** (2018), 77–100. https://doi.org/10.2140/memocs.2018.6.77

52. L. Placidi, E. Barchiesi, A. Misra, U. Andreaus, *Variational methods in continuum damage and fracture mechanics*, In: H. Altenbach, A. Öchsner, (eds) Encyclopedia of Continuum Mechanics, Berlin: Springer-Verlag, 2020. https://doi.org/10.1007/978-3-662-55771-6_172

53. L. Placidi, A. Misra, E. Barchiesi, Two-dimensional strain gradient damage modeling: a variational approach, *Z. Angew. Math. Phys.*, **69** (2018), 56. https://doi.org/10.1007/s00033-018-0947-4

54. A. Premchander, I. Amin, S. Oterkus, E. Oterkus, N. A. Shawky Elminshawy, Peridynamic modelling of propagation of cracks in photovoltaic panels, *Procedia Structural Integrity*, **41** (2022), 305–316. https://doi.org/10.1016/j.prostr.2022.05.036

55. A. Qinami, A. Pandolfi, M. Kaliske, Variational eigenerosion for rate-dependent plasticity in concrete modeling at small strain, *Int. J. Numer. Meth. Eng.*, **121** (2020), 1388–1409. https://doi.org/10.1002/nme.6271

56. Y. Rao, M. Xiang, J. Cui, A strain gradient brittle fracture model based on two-scale asymptotic analysis, *J Mech Phys Solids*, **159** (2022), 104752. https://doi.org/10.1016/j.jmps.2021.104752

57. Y. Rao, M. Xiang, Q. Li, J. Cui, A unified two-scale theory for modeling microstructural length scale, strain gradient and strain rate effects on brittle fracture, *Int J Solids Struct*, **268** (2023), 112176. https://doi.org/10.1016/j.ijsolstr.2023.112176

58. K. Ravi-Chandar, W. G. Knauss, An experimental investigation into dynamic fracture: I. Crack initiation and arrest, *Int J Fract*, **25** (1984), 247–262. https://doi.org/10.1007/BF00963460

59. K. Ravi-Chandar, W. G. Knauss, An experimental investigation into dynamic fracture: II. Microstructural aspects, *Int J Fract*, **26** (1984), 65–80. https://doi.org/10.1007/BF01152313

60. K. Ravi-Chandar, W. G. Knauss, An experimental investigation into dynamic fracture: III. On steady-state crack propagation and crack branching, *Int J Fract*, **26** (1984), 141–154. https://doi.org/10.1007/BF01157550

61. K. Ravi-Chandar, W. G. Knauss, An experimental investigation into dynamic fracture: IV. On the interaction of stress waves with propagating cracks, *Int J Fract*, **26** (1984), 189–200. https://doi.org/10.1007/BF01140627

62. N. Rezaei, E. Barchiesi, D. Timofeev, C. A. Tran, A. Misra, L. Placidi, Solution of a paradox related to the rigid bar pull-out problem in standard elasticity, *Mech Res Commun*, **126** (2022), 104015. https://doi.org/10.1016/j.mechrescom.2022.104015

63. N. Rezaei, M. E. Yildizdag, E. Turco, A. Misra, L. Placidi, Strain-gradient finite elasticity solutions to rigid bar pull-out test, *Contin. Mech. Thermodyn.*, **36** (2024), 607–617. https://doi.org/10.1007/s00161-024-01285-5

64. K. Shibanuma, S. Tu, S. Suzuki, Z. Yu, R. Kato, A. Hatamoto, Ductile crack propagation path depending on material properties: Experimental results and discussions based on numerical simulations, *Mater Design*, **223** (2022), 111158. https://doi.org/10.1016/j.matdes.2022.111158

65. Y. Solyaev, Steady-state crack growth in nanostructured quasi-brittle materials governed by second gradient elastodynamics, *Appl. Sci.*, **13** (2023), 6333. https://doi.org/10.3390/app13106333

66. Y. Solyaev, S. Lurie, H. Altenbach, F. dell'Isola, On the elastic wedge problem within simplified and incomplete strain gradient elasticity theories, *Int J Solids Struct*, **239–240** (2022), 111433. https://doi.org/10.1016/j.ijsolstr.2022.111433

67. D. Timofeev, E. Barchiesi, A. Misra, L. Placidi, Hemivariational continuum approach for granular solids with damage-induced anisotropy evolution, *Math Mech Solids*, **25** (2020), 738–770. https://doi.org/10.1177/1081286520968149

68. A. R. Torabi, K. Hamidi, A. S. Rahimi, S. Cicero, Notch fracture in polymeric specimens under compressive stresses: The role of the equivalent material concept in estimating the critical stress of polymers, *Appl. Sci.*, **11** (2021), 2104. https://doi.org/10.3390/app11052104

69. I. Vindokurov, Y. Pirogova, M. Tashkinov, V. V. Silberschmidt, Effect of heat treatment on elastic properties and fracture toughness of fused filament fabricated peek for biomedical applications, *Polymers*, **14** (2022), 2551. https://doi.org/10.3390/polym14245521

70. O. Wall, Dynamic crack propagation in large steel specimens, *Eng. Fract. Mech.*, **69** (2002), 835–849. https://doi.org/10.1016/S0013-7944(01)00111-4

71. P. Wu, F. Yang, Z. Chen, F. Bobaru, Stochastically homogenized peridynamic model for dynamic fracture analysis of concrete, *Eng. Fract. Mech.*, **253** (2021), 107863. https://doi.org/10.1016/j.engfracmech.2021.107863

72. J. Xu, D. Cao, J. Cui, X. Zhang, G. Li, Experimental research on tensile behavior of advanced high-strength steel dp600 at high strain rate, *J Mater Eng Perform*, **28** (2019), 2411–2420. https://doi.org/10.1007/s11665-019-04008-z

73. S. Yan, H. Yang, H. Li, G. Ren, Experimental study of macro-micro dynamic behaviors of 5A0X aluminum alloys in high velocity deformation, *Mat Sci Eng A-struct*, **598** (2014), 197–206. https://doi.org/10.1016/j.msea.2013.12.001

74. W. Yang, V. R. Sherman, B. Gludovatz, E. Schaible, P. Stewart, R. O. Ritchie, et al., On the tear resistance of skin, *Nat Commun*, **6** (2015), 6649. https://doi.org/10.1038/ncomms7649

75. M. E. Yildizdag, L. Placidi, E. Turco, Modeling and numerical investigation of damage behavior in pantographic layers using a hemivariational formulation adapted for a hencky-type discrete model, *Contin. Mech. Thermodyn.*, **35** (2023), 1481–1494. https://doi.org/10.1007/s00161-022-01154-z

76. M. E. Yildizdag, A. Ciallella, G. D'Ovidio, Investigating wave transmission and reflection phenomena in pantographic lattices using a second-gradient continuum model, *Math Mech Solids*, **28** (2023), 1776–1789. https://doi.org/10.1177/10812865221136250

77. B. Yin, M. Kaliske, Fracture simulation of viscoelastic polymers by the phase-field method, *Comput Mech*, **65** (2020), 293–309. https://doi.org/10.1007/s00466-019-01769-1

78. B. Zhang, J. Wang, Y. Wang, Y. Wang, Z. Li, Strain-rate-dependent tensile response of Ti-5Al-2.5Sn alloy, *Materials*, **12** (2019), 659. https://doi.org/10.3390/ma12040659

79. M. zhi Xing, Y. gang Wang, Z. xiu Jiang, Dynamic fracture behaviors of selected aluminum alloys under three-point bending, *Def Technol*, **9** (2013), 193–200. https://doi.org/10.1016/j.dt.2013.11.002

80. W. Zhong, I. Mbarek, A. Rusinek, R. Bernier, T. Jankowiak, G. Sutter, Development of an experimental set-up for dynamic force measurements during impact and perforation, coupling to numerical simulations, *Int. J. Impact Eng.*, **91** (2016), 102–115. https://doi.org/10.1016/j.ijimpeng.2016.01.006

81. G. Zou, C. Zhao, Z. Chang, W. Zhao, Y. Fan, S. Liu, et al., Experimental study on dynamic fracture toughness of compact tension specimens, *Exp Techniques*, **43** (2019), 57–64. https://doi.org/10.1007/s40799-018-0265-y